Periodically Poled Lithium Niobate for Visible Light Generation

CNF Project Number: 1997-11
Principal Investigator(s): Qiang Lin[1,2]
User(s): Jeremy Staffa[1]

Affiliation(s): 1. Institute of Optics, University of Rochester, Rochester NY;
2. Department of Electrical and Computer Engineering, University of Rochester, Rochester NY

Primary Source(s) of Research Funding: Defense Advanced Research Projects Agency (DARPA) LUMOS program under Agreement No. HR001-20-2-0044, the Defense Threat Reduction Agency-Joint Science and Technology Office for Chemical and Biological Defense (grant No. HDTRA11810047), and the National Science Foundation (NSF) (ECCS-1810169, ECCS-1842691, and OMA-2138174)

Contact: qiang.lin@rochester.edu, jstaffa@ur.rochester.edu

Website(s): https://arxiv.org/abs/2207.03071

Primary CNF Tools Used: JEOL 9500, AJA ion mill, CVC SC4500 odd-hour evaporator, Veeco Icon Atomic Force Microscope, DISCO Dicing Saw

Abstract:

We report efficient quasi phase matched second harmonic generation of 532 nm green light in periodically poled nanophotonic waveguides on the Lithium-Niobate on Insulator (LNOI) platform.

Summary of Research:

Visible light generation on an integrated photonic platform is of great interest for applications ranging across quantum optics, atomic physics, sensing, biophotonics, and AR/VR, to name a few. The (LNOI) platform boasts a broad transparency window, with low loss into the visible band [1], and exceptional quadratic optical nonlinearity for efficient conversion of long wavelength pump light into the visible spectrum [2,3]. Here we demonstrate efficient chip-scale generation of green light by second harmonic generation of a NIR source.

Quasi phase matched second harmonic generation of a 1064 nm pump source is realized by periodically poling the LN waveguide to bridge the phase mismatch between the 1064 nm and 532 nm optical modes. The fundamental TE_{00} modes are utilized for their near-unity nonlinear mode overlap and alignment with the largest quadratic nonlinear tensor element (d_{33} = 25pm/V) of LN. A relatively short poling period $\Lambda = \lambda_{SH}/\Delta n_{eff}$ of ~ 2.2 μm is necessary for quasi phase matching due to the difference in effective refractive indices Δn_{eff} of the TE_{00} modes. Poling with close to 50% duty cycle ensures optimal efficiency of the devices.

The PPLN waveguide devices are fabricated on MgO doped x-cut thin film lithium-niobate-on-insulator (LNOI), with 400 nm LN sitting upon a 2 μm silica layer. ZEP-520A resist is used for a first e-beam lithography step (JEOL 9500), followed by 300 nm Ar-ion milling (AJA Ion Mill) to create the alignment marks. A second e-beam writing step is performed on PMMA resist, and 300 nm poling electrodes are created using a gold evaporation and lift-off process (CVC SC4500 odd-hour evaporator). High voltage pulses realize the periodically inverted domains in the unprocessed LN thin film [4] and are verified by Piezo Response Force Microscopy (Veeco Icon AFM) (Figure 1b). The electrodes are removed in an acid clean step, and a third e-beam lithography step with ZEP-520A, followed again by Ar-ion milling, is used to define the waveguides along the periodically poled domains.

The 1064 nm light is amplified by a ytterbium-doped fiber amplifier and coupled to the waveguide facet by a 780HP lensed fiber. The residual pump light and generated visible light is collected from the output facet by a 780HP lensed fiber as well. A narrow $sinc^2$-like phase matching spectrum is observed (Figure 1d), indicating good uniformity of the periodically poled domains along the waveguide length. An absolute on-chip conversion efficiency in excess of 12% is measured with 16 mW of pump power, generating slightly more than 2 mW of green light on chip (Figure 1e). The sublinear efficiency trend agrees well with pump-depletion theory of colinear SHG, verifying strong pump conversion efficiency of the nonlinear waveguides.

References:

[1] Boris Desiatov, et al. "Ultra-low-loss integrated visible photonics using thin-film lithium niobate," Optica 6, 380-384 (2019).
[2] Cheng Wang, et al. "Ultrahigh-efficiency wavelength conversion in nanophotonic periodically poled lithium niobate waveguides," Optica 5, 1438-1441 (2018).
[3] Taewon Park, et al. "High-efficiency second harmonic generation of blue light on thin-film lithium niobate," Opt. Lett. 47, 2706-2709 (2022).
[4] Jonathan Tyler Nagy, et al. "Submicrometer periodic poling of lithium niobate thin films with bipolar preconditioning pulses," Opt. Mater. Express 10, 1911-1920 (2020).

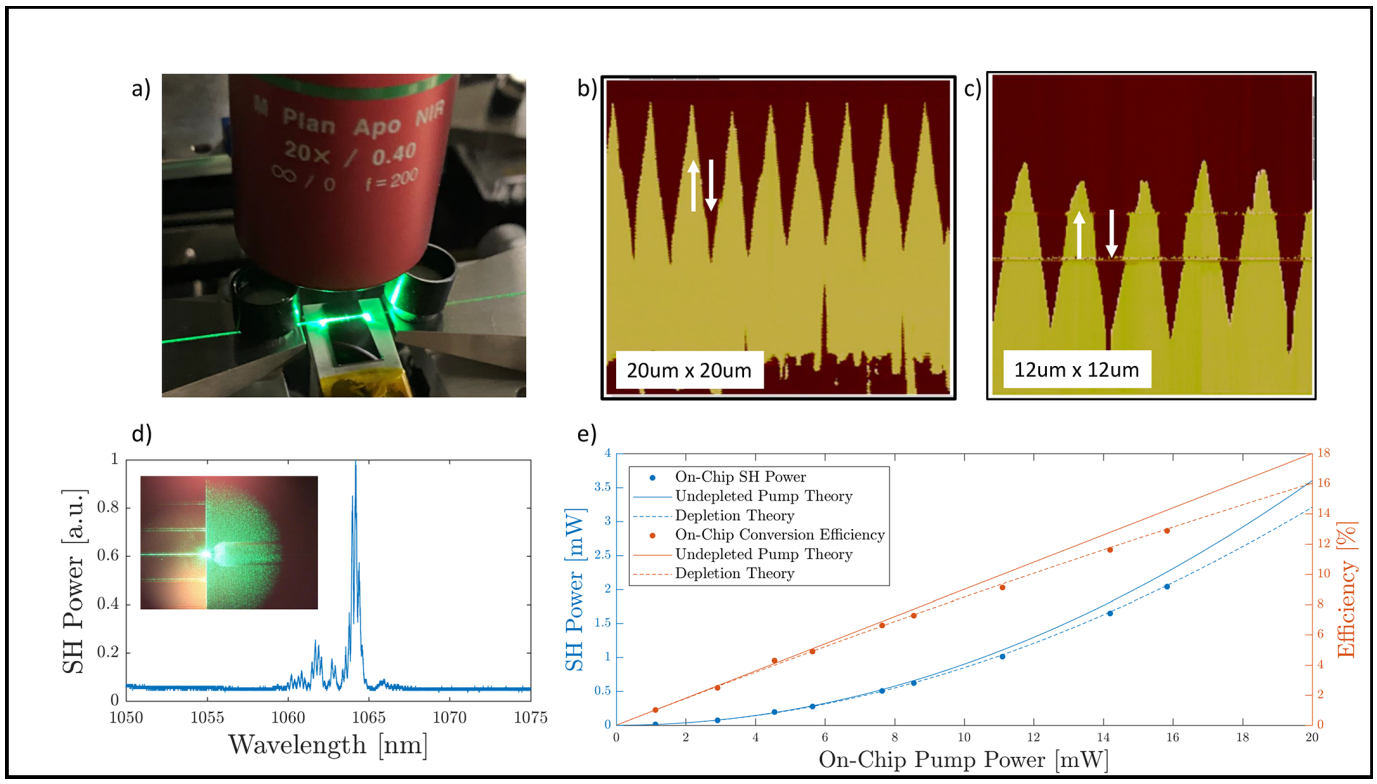

Figure 1: (a) Image of efficient green light generation on the PPLN chip. Piezo Response Force Microscopy of the periodically inverted domains before (b) and after (c) waveguide fabrication. (d) Measured phase matching spectrum of the device, centered around 1064 nm. (e) On-chip conversion efficiency and generated visible light power from the quasi phase matched SHG process.

Full-Spectrum Visible Electro-Optic Modulator

CNF Project Number: 1997-11
Principal Investigator(s): Qiang Lin
User(s): Shixin Xue, Jingwei Ling, Jeremy Staffa, Qili Hu, Zhengdong Gao

Affiliation(s): Department of Electrical and Computer Engineering, University of Rochester; Institute of Optics, University of Rochester

Primary Source(s) of Research Funding: Meta Platform Technologies LLC; Defense Advanced Research Projects Agency (LUMOS, HR001-20-2-0044)

Contact: qiang.lin@rochester.edu, sxue4@ur.rochester.edu, jling8@ur.rochester.edu, jstaffa@u.rochester.edu, qhu17@ur.rochester.edu, zgao14@ur.rochester.edu

Primary CNF Tools Used: JEOL JBX9500FS Electron-Beam Lithography System, Odd Hour Evaporator, AJA Ion Mill, Zeiss Ultra SEM

Abstract:

We report an on-chip high-speed visible-band electro-optic modulator that can operate over the full visible spectrum of 400-700 nm, with a record low $V\pi{\cdot}L$ of 0.48, 0.25, and 0.17V·cm at red, green, and blue wavelengths of 630, 520, and 450 nm, respectively, and an operation bandwidth of > 20 GHz.

Summary of Research:

The visible spectral region underpins many important applications including sensing, optical clocks, 3D displays, and augmented/virtual reality (AR/VR). All of these applications rely crucially on precise control and efficient modulation of visible light. Recently, there has been significant interest in transferring these applications onto chip-scale platforms [1,2] that would offer great advantages in size, power, functionality, and design flexibility. However, development of chip-scale electro-optic modulators (EOMs) in the visible band remains fairly limited [3-5]. Here, we demonstrate an on-chip lithium niobate (LN) EOM that can operate over the full spectrum covering the entire visible band from 400 to 700 nm. We show that the visible-band EOM exhibits record high modulation efficiency with $V\pi{\cdot}L$ as low as 0.48, 0.25, and 0.17V·cm at wavelengths of 630, 520, and 450 nm, respectively, which are the smallest ever reported for LN traveling-wave EOMs developed to date.

Figure 1(a) shows a fabricated EOM that consists of a pair of 3 dB multimode interference (MMI) couplers, an 8-mm-long phase modulation section operating in the push-pull fashion, and a spatial-mode filter section placed in the front.

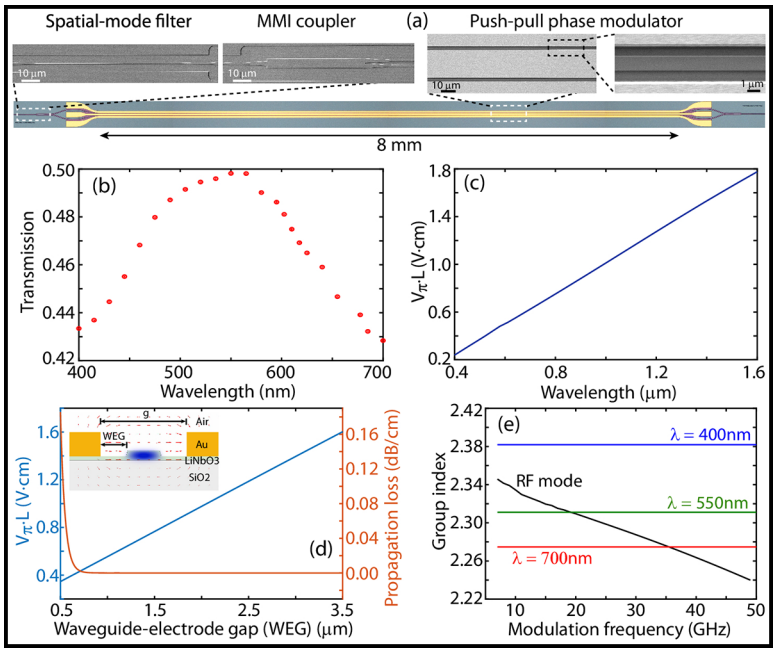

The devices are made on a 300-nm-thick x-cut LN-on-insulator wafer, partially etched down by 180 nm. The modulator waveguide has a width of 1 μm and a waveguide-electrode gap (WEG) of 0.8 μm, with an electrode spacing of 2.6 μm in order to enhance modulation efficiency. The electrodes contact directly with the LN layer to improve the optical-microwave mode overlap. For the EOM to operate over the full visible spectrum, the MMI coupler is designed to be broadband with a transmission of 43.3%, 49.8%, and 42.8% at wavelengths of 400, 550, and 700 nm, respectively [Figure 1(b)]. The SMF is a tapered waveguide to cut off higher-order guided modes to ensure single-mode operation of the EOM.

Figures 2(a)-2(c) show the modulation performance of the EOM. The device exhibits a $V\pi$ of 0.60 V, 0.31 V, and 0.21 V, respectively, at the red, green, and blue wavelengths of 630, 520, and 450 nm, which corresponds to a $V\pi{\cdot}L$ of 0.48, 0.25, and 0.17V·cm. The extinction ratio (ER) is measured to be 16 dB at 630 nm [Figure 2(a)]. The ER decreases to 7 dB and 12 dB at 520 and 450 nm [Figures 2(b) and 2(c)], respectively, which is dominantly due to the green and blue FP lasers (Thorlabs, LP-520 and LP-450) with a poor polarization ER of ~ 10 dB that interferes with the ER characterization. The recorded WEG dependence of $V\pi{\cdot}L$ [Figure 2(d)] shows a slightly better performance than the theoretical expectation, which is likely due to a smaller fabricated WEG than the designed WEG. Figure 2(e) shows that the EOM exhibits a 3 dB bandwidth of 16 GHz (blue curve). This value is simply limited by the frequency response of the optical detector (Newport, 1544-B) [Fig. 2(e), red curve]. By factoring out the detector response, the EOM itself exhibits a 3 dB bandwidth > 20 GHz [Fig. 2(e), green curve]. The insertion loss of the EOM is measured to be 6.8 dB at 630 nm, which is primarily attributed to the fabrication imperfections of the SMF and the MMI couplers.

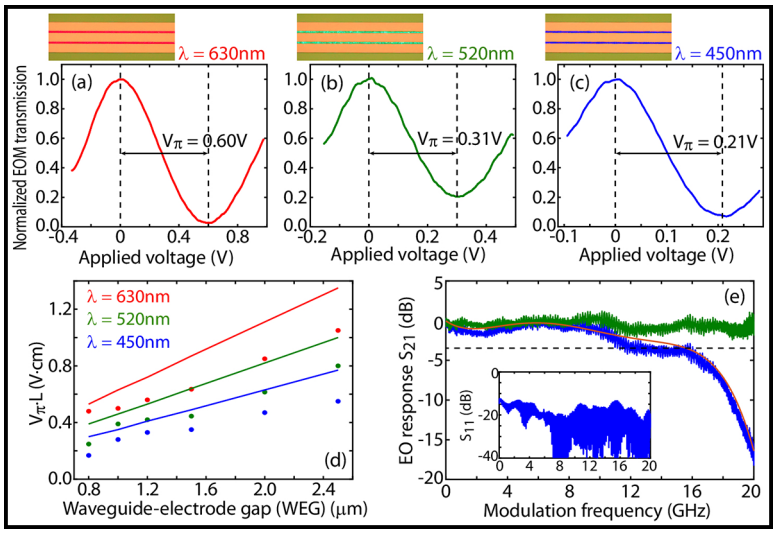

The demonstrated full-spectrum EOM with record performance achieves a key step toward energy-efficient and high-speed visible photonics, opening up a great avenue toward chip-scale miniaturization and integration of versatile functionalities in sensing, atomic clocks, AR/VR, etc., on the promising thin-film LN platform.

References:

[1] T. J. Morin, L. Chang, W. Jin, C. Li, J. Guo, H. Park, M. A. Tran, T. Komljenovic, and J. E. Bowers, Optica 8, 755 (2021).

[2] M. Dong, G. Clark, A. J. Leenheer, M. Zimmermann, D. Dominguez, A. J. Menssen, D. Heim, G., Gilbert, D. Englund, and M. Eichenfield, Nat. Photonics 16, 59 (2022).

[3] B. Desiatov, A. Shams-Ansari, M. Zhang, C. Wang, and M. Lon.ar, Optica 6, 380 (2019).

[4] O. T. Celik, C. J. Sarabalis, F. M. Mayor, H. S. Stokowski, J. F. Herrmann, T. P. McKenna, N. R. Lee, W. Jiang, K. K. Multani, and A. H. Safavi-Naeini, Opt. Express 30, 23177 (2022).

[5] C. Li, B. Chen, Z. Ruan, H. Wu, Y. Zhou, J. Liu, P. Chen, K. Chen, C. Guo, and L. Liu, Opt. Express 30, 36394 (2022).

Monolithic Ultrabroadband Multispectral Color Filter Array

CNF Project Number: 2524-17
Principal Investigator(s): Jaime Cardenas
User(s): Jiewei Xiang

Affiliation(s): The Institute of Optics, University of Rochester

Primary Source(s) of Research Funding:

Contact: jaime.cardenas@rochester.edu, jxiang6@ur.rochester.edu

Website(s): https://www.hajim.rochester.edu/optics/cardenas/

Primary CNF Tools Used: ASML stepper, Oxford 100 ICP-RIE, YES EcoClean Asher, Oxford PECVD, JEOL 9500, Heidelberg Mask Writer-DWL2000, ABM Contact Aligner, Oxford Cobra ICP Etcher, Woollan RC2 Spectroscopic Ellipsometer, Logitech Orbis CMP, AJA Sputter System

Abstract:

We use a modified Fabry-Perot structure with selectively suppression and subwavelength structures in cavity to realize MSFAs that can cover the range from 450 - 910 nm.

Summary of Research:

Multispectral imaging (MSI) has found applications in various fields such as metrology, medical spectrum diagnoses, and industrial processes, offering scenes with multiple narrowband spectral channels. Conventional multispectral systems typically rely on dispersive elements like diffraction gratings or prisms, which limit further miniaturization and integration [1]. To overcome this limitation, snapshot multispectral imaging systems based on multispectral filter arrays (MSFAs) have been developed [2]. These systems enable the capture of a parallel array of images with different spectral channels in a single shot, eliminating the need for spatial or spectral scanning and allowing for highly compact and integrated designs. However, the design and fabrication of a monolithic broadband MSFA with narrow bandwidth and high color purity present significant challenges.

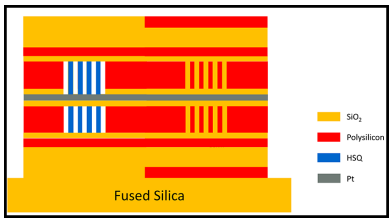

Figure 1: Schematic of the stack structure of the color filters.

People have demonstrated integratable color filter arrays (CFAs) using various approaches such as plasmonic resonance [3], Mie resonance [4], and guided mode resonance [5]. Among these, CFAs based on Fabry-Perot (FP) resonators offer advantages such as polarization insensitivity, angle insensitivity, high transmission, and narrow full-width at half-maximum (FWHM), which are desirable for multispectral filter arrays (MSFAs). However, traditional thin film color filter arrays based on FP cavities often require multiple filter stacks, leading to fabrication challenges and limited spectral range [6]. Increasing the number of detection channels also necessitates additional lithography and etching steps, further complicating the fabrication process. To address these challenges, subwavelength grating structures have been introduced to modify the optical length of the cavity without altering the physical thickness. Nevertheless, in FP resonators, multiple resonances can impact color purity and the free spectral range (FSR). Furthermore, the spectral tuning range is restricted by the nanofabrication process, as the fill ratio of the subwavelength grating cannot be excessively high.

We present a CMOS compatible multispectral FP color filter arrays which have a large spectral range (450nm-910nm) with narrow FWHM (<40nm) based on selective suppression and a subwavelength grating (Figure 1). We demonstrate the broadband MSFAs based on modified FP structure with second order resonance which can cover the wavelength range from 630 nm to 960 nm [7]. One of the limitations of extending the color filters to shorter wavelength is the effective index range that can be obtained with polysilicon and silicon dioxide subwavelength structures. To extend the working wavelength range to cover visible spectra, we enlarge the effective index range by introducing air in the cavity. To cap air in the cavity, we need the air gaps in the cavity have a relatively small feature size and high aspect ratio such that we can cap as much as air in the cavity rather than fill it out with top deposition. To circumvent the high aspect ratio etch step, we directly use 11% HSQ as the cavity layer and expose the HSQ layer with hexagonal subwavelength grating or mesh structures. After development, we can have around 50 nm width and 170 nm depth air gaps without the need of high aspect ratio etching. We cap the air with top deposition based

on the filling capability of deposition recipe. To enhance the transmission, we use one 35 nm layer as the reflection mirror. We combine the HSQ and air cavity design with the polysilicon and silicon dioxide cavity design such that we can cover the range from visible to NIR.

The main fabrication steps for our design are shown in Figure 2. We use polysilicon as the high index material in the DBRs. Polysilicon is deposited by plasma-enhanced chemical vapor deposition (PECVD) and anneal it at 700°C for two hours to make it crystalize. We use JEOL 9500 and negative resist hydrogen silsesquioxane (HSQ) to pattern the cavity and use inductively coupled plasma reactive ion etching with HBr to transfer the pattern from HSQ to polysilicon. We fill the gap by TEOS (Tetraethyl orthosilicate) SiO_2. After finishing the fabrication of long polysilicon and silicon dioxide cavity, we etched away the silicon dioxide for the area with HSQ and air cavity. The 11% HSQ is spun at 2000 rpm to have around 210 nm thickness. After exposure and development, we use PECVD to deposit silicon dioxide to cap the air gaps and use chemical mechanical polishing (CMP) to planarize the surface. We anneal our sample to make HSQ turn into silicon dioxide material. After testing, there is about 20% thickness decrease after annealing. However, there is no obvious lateral dimension change or structure deformation (Figure 3). Through the similar processes we can fabricate the top part of our design.

We present a broadband multispectral color filter arrays covering from 450 nm to 910 nm with transmissions over 40% and FWHM less than 40 nm (Figure 4). The simulation is based on Rigorous coupled-wave analysis (RCWA). To overcome the effective index range limitations, we lower the cavity effective index by mixing air with silicon dioxide. To alleviate the fabrication challenges, we use the e-beam resist HSQ as the cavity layer which is close to silicon dioxide after annealing. We show that the patterned HSQ will not have obvious deformation after annealing at 700°C which make it a good alternative for silicon dioxide when pattern relatively small features.

Conclusion and Future Steps:

We present a MSFAs design that can cover the wavelength range from 450 nm to 910 nm aligned with the detection range of most silicon CMOS imaging sensors. We demonstrate the potential of using HSQ directly as a part of nanostructure which can have relatively small feature size after development and have similar optical property as silicon dioxide after anneal. With the HSQ and air cavity, the effective index range is extended which enables monolithic MSFAs to cover a wavelength range from visible to NIR.

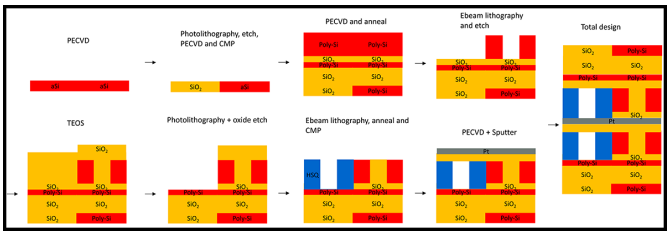

Figure 2: The main fabrication steps.

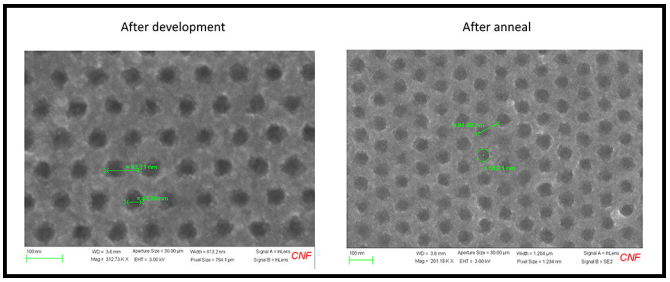

Figure 3: SEM images of patterned HSQ layers after development and anneal.

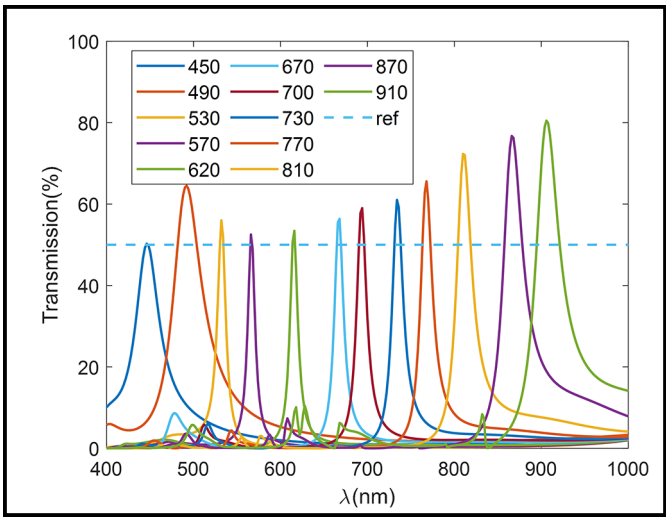

Figure 4: The relative transmission of different color filters based on simulation.

References:

[1] Lapray, P.-J., et al. Multispectral Filter Arrays: Recent Advances and Practical Implementation. Sensors 14, 21626-21659 (2014).

[2] McClung, A., et al. Snapshot spectral imaging with parallel metasystems. Sci. Adv. 6, eabc7646 (2020).

[3] Xu, T., et al. Plasmonic nanoresonators for high-resolution colour filtering and spectral imaging. Nat. Commun. 1, 59 (2010).

[4] Dong, Z., et al. Printing Beyond sRGB Color Gamut by Mimicking Silicon Nanostructures in Free-Space. Nano Lett. 17, 7620-28 (2017).

[5] Ferraro, A., et al. Guided-mode resonant narrowband terahertz filtering by periodic metallic stripe and patch arrays on cyclo-olefin substrates. Sci Rep 8, 17272 (2018).

[6] Park, C., Shrestha, V., Lee, S., and Choi, D., Trans-Reflective Color Filters Based on a Phase Compensated Etalon Enabling Adjustable Color Saturation. Scientific Reports 6, 25496 (2016).

[7] Xiang, J., Song, M., Zhang, Y., Kruschwitz, J., and Cardenas, J. Broadband tunable, narrow linewidth multispectral color filter. in Frontiers in Optics + Laser Science 2022 (FIO, LS) (2022).

High-Quality-Factor SiN Ring Resonator of 12 GHz Repetition Rate

CNF Project Number: 2524-17
Principal Investigator(s): Jaime Cardenas
User(s): Yi Zhang

Affiliation(s): The Institute of Optics, University of Rochester

Primary Source(s) of Research Funding: National Science Foundation

Contact: jaime.cardenas@rochester.edu, yzh239@ur.rochester.edu
Website(s): https://cardenaslabphotonics.com/

Primary CNF Tools Used: JEOL 9500, ASML PAS 5500/300C DUV Stepper, Oxford PECVD, PT Takachi HDP-CVD, LPCVD Furnace, Oxford 100 ICP Dielectric Etcher, Unaxis 770 Deep Silicon Etcher, PT Deep Silicon Etcher, YES EcoClean Asher, Xactix Xenon Difluoride Etcher

Abstract:

We demonstrate a high-quality-factor silicon nitride ring resonator of 12 GHz repetition rate. Special fabrication techniques are applied to acquire an intrinsic quality factor of 10 million as well as anomalous dispersion (for fundamental modes) in the resonator.

Summary of Research:

Silicon nitride (Si_3N_4) [1] is a high-performance material platform for chip-scale photonic devices. Benefiting from its ultra-low loss and good CMOS-compatibility, Si_3N_4 is a preferable choice for making waveguides, resonators, and other passive components for photonic integrated circuits (PICs). In addition, Si_3N_4 supports not only applications in the optical communications band but also in the visible [2] and the mid-infrared band, such as (bio)medical and (bio)chemical sensing, due to its broad transparency window (400-6700 nm [3]).

Ring resonator is one of the fundamental components in integrated photonics. It can work for versatile purposes, including laser cavity, modulator, filter, etc. In this work, we design and fabricate a Si_3N_4 ring resonator with anomalous dispersion (for fundamental modes) for generating dissipative Kerr solitons (DSK) [4]. The resonator has a cross-section of 1.6 μm × 0.76 μm. Such a structure supports a very confined fundamental transverse electric (TE0) mode (inset in Figure 1) and, therefore, leads to an anomalous dispersion [5].

We design the cavity length of the resonator to be 11.6 mm and have a repetition rate (the inverse of its round-trip time) of 12.3 GHz according to $T_R = L/c_0 n_g$ where T_R is the round-trip time, L is the cavity length, c_0 is the light speed in vacuum, and n_g is the group index of the guide mode (2.11 for TE_0 mode in our case). This repetition rate allows the incorporation of the generated solitons with radio frequency (RF) applications. Figure 1 shows a fabricated device.

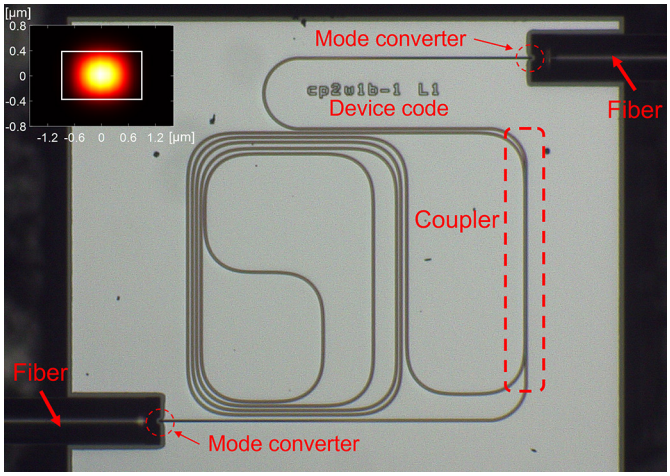

Figure 1: Camera picture of a fabricated device. Inset: TE_0 mode of the device.

We use adiabatic turnings in our spiral-like ring resonator to minimize the bending loss. The radius of curvature of the waveguide smoothly changes from 3 mm to 0.1 mm through a tanh function [6] instead of a conventional abrupt turning of fixed radius. We use SiO_2 mode converters [7] and tapered Si_3N_4 waveguides (Figure 2(c)) to optimize the power coupling efficiency from the fiber to the device.

The fabrication steps are shown in Figure 2(a-b). We deposit 0.76 μm stoichiometric Si_3N_4 using low pressure vapor chemical deposition (LPCVD) over 4 μm of thermally-grown silicon oxide (SiO_2) on silicon wafer. We rotate the wafer by 45° after every 300 nm deposition to alleviate the total strain accumulated in the film and prevent it from cracking [8]. We pattern the device using 100 kV electron-beam lithography. The pattern is exposed twice with half of the required dose each time ('double pass') for better lithography accuracy and better sidewall roughness. We etch the structure

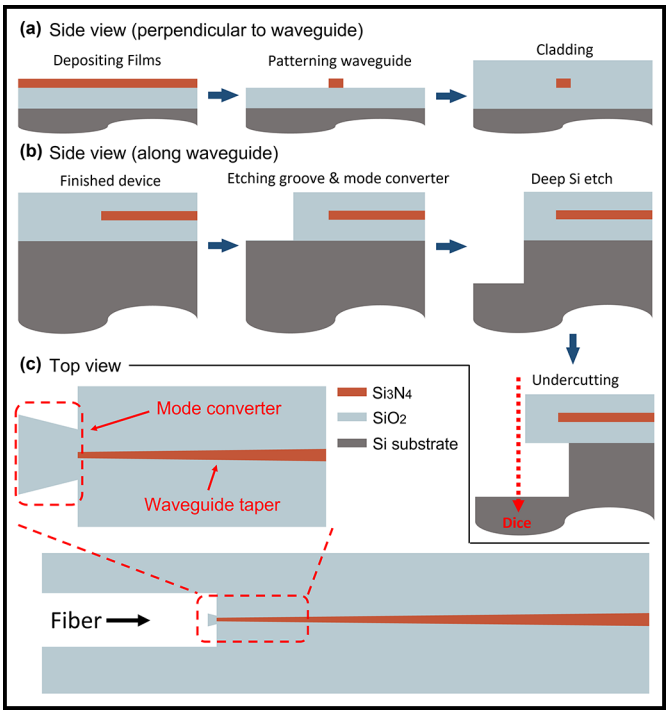

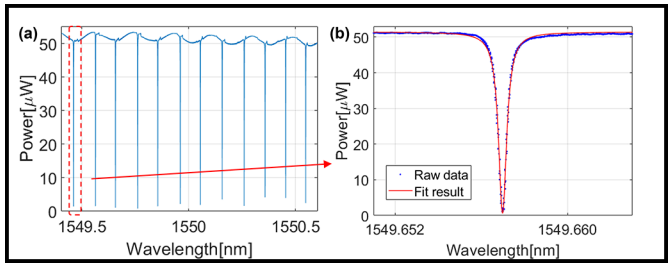

Figure 2, left: (a-b) Fabrication procedures of the device. (c) A zoom-in view of the waveguide taper and the mode converter.

Figure 3, above: (a) Measured typical transmission spectrum of the device. (b) Typical fitting result of a resonance.

with inductively coupled plasma reactive-ion etching (ICP-RIE). The etched structures are then clad with 4 μm SiO_2 through plasma-enhanced chemical vapor deposition (PECVD). Afterward, we pattern the mode converters and the grooves, which are used to ensure stable fiber-to-chip power coupling, with deep ultraviolet (DUV) lithography. The SiO_2 outside the chip boundary is etched using ICP-RIE. We continue to etch down the exposed Si substrate by approximately 100 μm using a Bosch process so that fibers can be pushed all the way to the mode converter (vertically aligned) after dicing without being blocked by the substrate. We anneal the device at 1200°C to improve the material quality and mitigate the material loss. Finally, we use the isotropic XeF_2 etch to remove the Si beneath the mode converter and make it suspended after dicing the wafer into chips.

We then measure the transmission spectrum (Figure 3(a)) of the fabricated device and characterize its performance. Figure 3(a) shows a typical spectrum. We numerically fit (Figure 3(b)) the resonances in the spectrum using a Lorentzian equation [9]

$$T = T_0 \frac{(a-t)^2 + \frac{4at\pi^2}{FSR^2}(\lambda-\lambda_0)^2}{(1-at)^2 + \frac{4at\pi^2}{FSR^2}(\lambda-\lambda_0)^2}$$

where T stands for power transmission, T_0 is a constant, t is the field transmission of the coupler, a is the round-trip field transmission of the ring, FSR is the free spectral range, λ is the testing laser wavelength, and λ_0 is the central wavelength of the resonance. The round-trip is approximately 1% across the 1480-1640 nm bandwidth, which corresponds to a propagation loss of 0.04 dB/cm and an intrinsic quality factor of 10 million in our 11.6 mm ring.

We further extract the group index and the group velocity dispersion of the device (TE_0) to be 2.11 (corresponding to 12.3 GHz repetition rate) and -1.84 × 10^5 fs^2/m, respectively.

Conclusions and Future Steps:

In conclusion, we demonstrate a silicon nitride ring resonator with anomalous dispersion, 12.3 GHz repetition rate, and 10 million intrinsic quality factor. This work will help to enable RF-frequency applications directly based on high-performance Si_3N_4 ring resonators.

References:

[1] Blumenthal, Daniel J., et al. "Silicon nitride in silicon photonics." Proceedings of the IEEE 106.12 (2018): 2209-2231.

[2] Porcel, Marco AG, et al. "Silicon nitride photonic integration for visible light applications." Optics & Laser Technology 112 (2019): 299-306.

[3] Soref, Richard. "Mid-infrared photonics in silicon and germanium." Nature photonics 4.8 (2010): 495-497.

[4] Kippenberg, Tobias J., et al. "Dissipative Kerr solitons in optical microresonators." Science 361.6402 (2018): eaan8083.

[5] Foster, Mark A., et al. "Broad-band optical parametric gain on a silicon photonic chip." Nature 441.7096 (2006): 960-963.

[6] Ji, Xingchen, et al. "Exploiting ultralow loss multimode waveguides for broadband frequency combs." Laser & Photonics Reviews 15.1 (2021): 2000353.

[7] Nauriyal, Juniyali, et al. "Fiber-to-chip fusion splicing for low-loss photonic packaging." Optica 6.5 (2019): 549-552.

[8] El Dirani, Houssein, et al. "Crack-free silicon-nitride-on-insulator nonlinear circuits for continuum generation in the C-band." 2018 IEEE Photonics Conference (IPC). IEEE, 2018.

[9] Cardenas, Jaime, et al. "High Q sic microresonators." Optics express 21.14 (2013): 16882-16887.

Ultrathin Infrared Photonic Devices Based on Semiconductor-Metasurfaces

CNF Project Number: 2979-21
Principal Investigator(s): Gennady Shvets
User(s): Melissa Bosch

Affiliation(s): School of Applied and Engineering Physics, Department of Physics; Cornell University
Primary Source(s) of Research Funding: Office of Naval Research (ONR), National Science Foundation (NSF)
Contact: gs656@cornell.edu, mb2583@cornell.edu
Website(s): http://shvets.aep.cornell.edu
Primary CNF Tools Used: JEOL 9500, Zeiss Ultra SEM, Oxford 100 Etcher, Oxford PECVD, Woollam RC2 Ellipsometer

Abstract:

Metasurfaces, composed of planar arrays of sub-wavelength-scale optical antennae, provide tailored resonant modulations to electromagnetic fields. We fabricate semiconductor-based metasurfaces fit for a range of photonic applications in the near-and mid-infrared. For instance, we apply an amorphous silicon (aSi) metasurface to demonstrate an ultrathin wide-aperture multicolor lens. In another application, we exploit tailored field enhancements of silicon-on-sapphire (SOI)-metasurfaces to facilitate deeply-subwavelength femtosecond (fs) laser machining.

Multicolor aSi-Metalens:

Modern imaging systems rely on compact, wide-aperture, and aberration-free lenses. Although submicron-thick optical metasurfaces have achieved high-performance focusing [1], they exhibit high chromatic aberrations, making them unsuitable multicolor imaging applications. Various approaches to achromatic metalensing have been developed [2], but they are typically limited by computational complexity or low numerical aperture (NA). Our project considers a new type of high-NA multi-color metalens, engineered to reuse identical discrete phase requirements in every consecutive 2π phase increment (Fresnel zone) of its phase profile, thereby significantly simplifying its design. To test this concept, we fabricated a spherical metalens with a diameter of 1 mm. Figure 1(a) shows a representative scanning electron microscope of the building blocks of the metalens, which are 600-nm-thick rectangular aSi bricks arranged periodically on a silica substrate. These structures support Mie-type optical resonance modes that can be customized by altering the resonator's geometrical parameters. The metalens comprises only fifteen distinct resonator geometries that are optimized to provide a wavelength- and radially-dependent phase profile resulting in the multicolor focusing of two near-infrared wavelengths. Metalens fabrication consisted of six total steps: plasma-enhanced chemical vapor deposition (Oxford PECVD) of aSi onto fused silica substrate; HSQ-6% spincoat, baking, and electron beam lithography (EBL) exposure at 6mC/cm^2 (JEOL9500FS); development in TMAH/NaCl (0.25/0.7N) salty solution; and pattern transfer to the aSi layer through an inductively coupled HBr plasma reactive ion etch (Oxford Cobra). The resulting samples were characterized using a scanning electron microscope (Zeiss Ultra). Our simulations predict diffraction-limited and chromatic-aberration-free focusing of the two operation wavelengths at a focal distance of z = 5 mm. The experimental characterization of our first-generation device shows a primary focal spot at the predicted z-position (5mm) for both wavelengths of light (as shown in Figure 1b). However, there are a few unintended spurious maxima appearing at different z-positions. The production of improved devices is underway.

Subwavelength fs-Laser Nanomachining using SOI-Metasurfaces:

In a second application, we employ tailored electromagnetic field distributions of resonant semiconductor microstructures to enhance the spatial resolution and control of laser-nanostructuring. While laser-machining approaches are typically restricted by the diffraction limit to yield a smallest resolvable dimension equal to half the laser wavelength [3], our project considers deeply-subwavelength-scale ($\sim\lambda/50$) modifications to Si-based microresonators illuminated

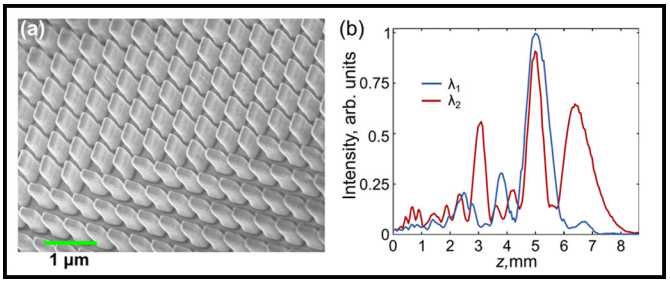

Figure 1: (a) A zoomed-in scanning electron microscopy (SEM) image of rectangular aSi pillars on a silica substrate, comprising the aSi metalens. (b) Experimental on-axis intensity of light transmitted through a first-generation multicolor aSi-metalens. The lens focuses wavelengths of λ_1 = 980 nm (blue line) and λ_2 = 735 nm (red line) into a primary intensity maximum at z = 5 mm.

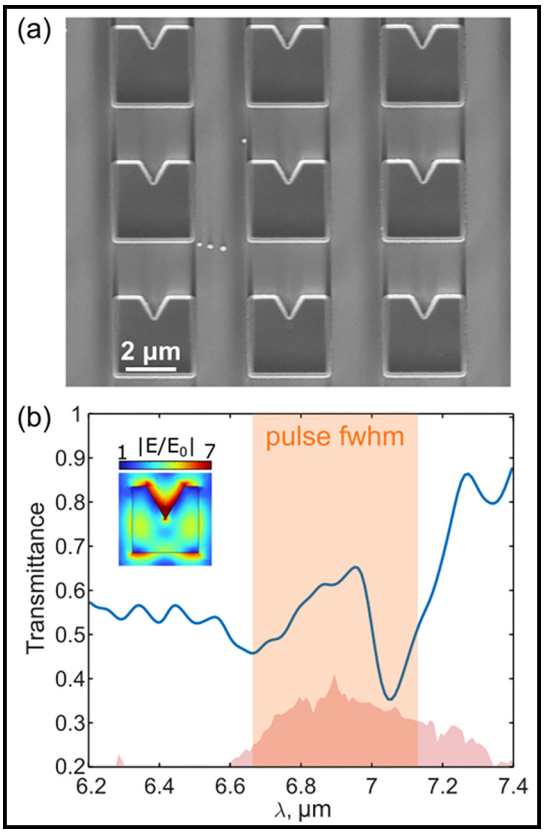

Figure 2: (a) SEM image of a SOI-metasurface designed to enhance the field intensity at the apex of its triangular notch. (b) Representative experimental transmission spectra of the metasurface. Inset: simulated electric field profile of the resonator.

by fs laser pulses. We accomplish this result by designing SOI metasurfaces that resonate near the laser wavelength and exhibit highly-nonlinear photoinduced free carrier production. Illuminating the Si-resonators with few-pulse trains below the single-pulse damage threshold facilitates localized phase explosions and gradual volumetric material ablation in the region of peak field intensity. For device fabrication, we start with the RIE etching of a commercial SOI wafer to the desired thickness, followed by a standard PMMA spin-coat, baking, EBL exposure at 900 μC/cm^2 (JEOL 9500FS), development in MIBK:IPA 1:3 for 90s, e-beam evaporation of 30 nm chromium (Cr) or 80 nm alumina hard mask (CVC SC4500), liftoff in room-temperature sonicated acetone for 30 min, RIE etching to substrate; and removal of Cr or alumina mask by wet etchant. Figure 2 presents an SEM image of the fabricated metasurface prior to laser irradiation alongside its experimental transmission spectra. Figure 3 shows examples of nanotrench formation under various conditions of laser pulse intensity and number.

References:

[1] Pan, Meiyan, et al. Light: Science & Apps 11.1 (2022): 195.
[2] Wang, Shuming, et al. Nature Nanotech 13.3 (2018): 227-232.
[3] Perry, M. D. et al., Journal of Applied Physics 85, 6803 (1999).

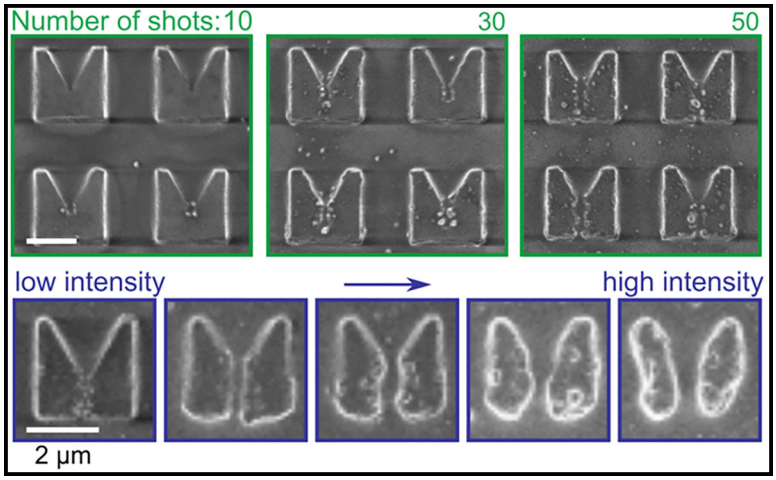

Figure 3: Trench formation in SOI-resonator arrays illuminated with variable (a) shot-numbers and (b) intensities of 7 µm-wavelength incident laser pulses, increasing from left to right.

HfO_2-Based Platform for High Index Contrast Visible and UV Integrated Photonics

CNF Project Number: 2985-21
Principal Investigator(s): Karan Kartik Mehta[2]
User(s): Oscar Jaramillo[1,2], Joshua Tensuan[2]

Affiliation(s): 1. School of Applied and Engineering Physics,
2. School of Electrical and Computer Engineering; Cornell University

Primary Source(s) of Research Funding: Cornell University

Contact: karanmehta@cornell.edu, oj43@cornell.edu

Primary CNF Tools Used: Metricon, Zeiss Ultra SEM, JEOL 9500, PT770 Etcher, WoollamRC2 Spectroscopic Ellipsometer, AFM, Furnace, Oxford PECVD, Oxford FlexAL

Abstract:

We study HfO_2/Al_2O_3 composites for high-index visible/ultraviolet photonics, exhibiting single-mode waveguides losses of 1.9 ± 1 dB/cm for λ = 405 nm.

Summary of Research:

Integration of photonic devices in the visible and UV is necessary for several applications such as spectroscopy and control of ion systems on chip [1-3]. However, photonic devices operating in the visible and UV have lagged behind those operating in the near infrared devices since common materials used in photonic devices absorb at short wavelengths, and scattering losses increase as wavelengths decrease.

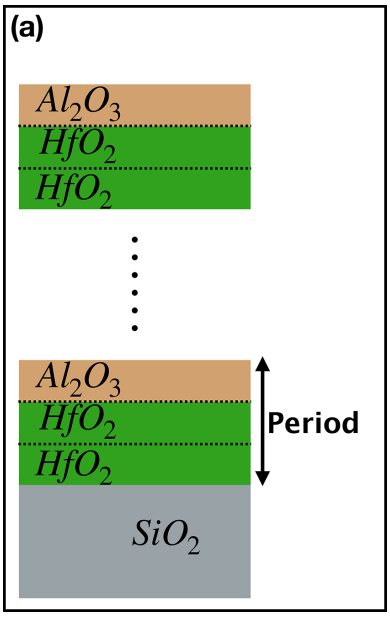

Figure 1: Single layers of HfO_2 and Al_2O_3 are deposited on top of SiO_2 in an inter-layered periodic way. A DC = 0.33 is shown here with P=3 layers.

Alumina (Al_2O_3) is a CMOS compatible material that can be deposited in amorphous form, and has been used to demonstrate single-mode (SM) propagation as low as 3 dB/cm at 371 nm [4]; however, its relatively low index (n~1.7) is a limitation. High refractive index is desirable in many settings since it allows, for example, strong optical confinement, compact device footprints, high efficiency grating devices (grating strengths scale approximately as $\sim (n_{core}^2 - n_{cladding}^2)^2$), and efficient acousto-optic interaction (scaling as n^6). HfO_2 is promising material — a wide band-gap (5.65 eV) [5] with a high refractive index (n~2.1), can be deposited amorphously, and is CMOS compatible. However, its propensity to crystallize results in significant optical loss, and its use in photonics has been limited to settings where the optical interaction length is on the order of 100s of nm [6,7]. Incorporation of moderate proportions of Al_2O_3 dramatically reduces losses in films; this is attributed to inhibited crystallization of HfO_2 [8]. Here, we demonstrate methods to lithographically pattern nanophotonic structures composed of alternating layers of Al_2O_3 and HfO_2, deposited via atomic layer deposition (ALD), and present preliminary SM propagation losses in patterned waveguides formed from the composite.

Our approach to mitigating loss from crystallization relies on depositing alternating HfO_2 and Al_2O_3 layers at different duty cycles (DC) and periods (P) in a plasma enhanced ALD (PEALD) process. Figure 1 shows the structure of the composite films; P represents the total number of layers per period, with DC the fraction of atomic layers per period that are Al_2O_2. Previous work [8], showed that as the DC changes from 0 (HfO_2 only) to 1 (Al_2O_3 only), the refractive index decreases as if the index of the composite was the weighted average of n(Al_2O_3) and n(HfO_2) according to fractional composition. Measurements of slab mode propagation loss at λ = 406 nm by the prism coupling method showed that losses can be 4.2 dB/cm for a period of three layers and a DC ~ 0.3. In contrast, losses in pure HfO_2 at this wavelength were well above 30 dB/cm. The observed decrease in loss is accompanied by a reduction in index to n = 1.95, though still preserving most of HfO_2's advantage over Al_2O_3.

Work to pattern the composite material into photonic devices was conducted at the Cornell NanoScale Facility (CNF). Devices were fabricated on a silicon wafer with

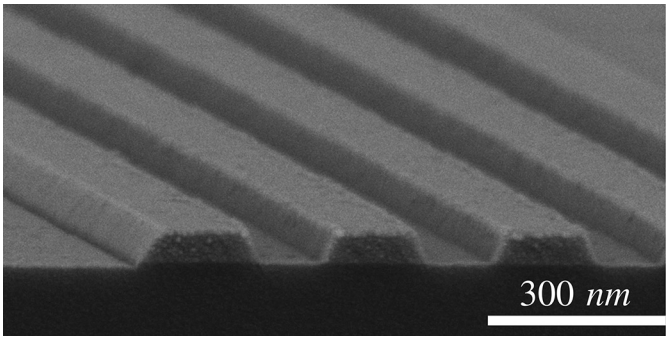

Figure 2: SEM image of ridges etched into the composite films as test structures.

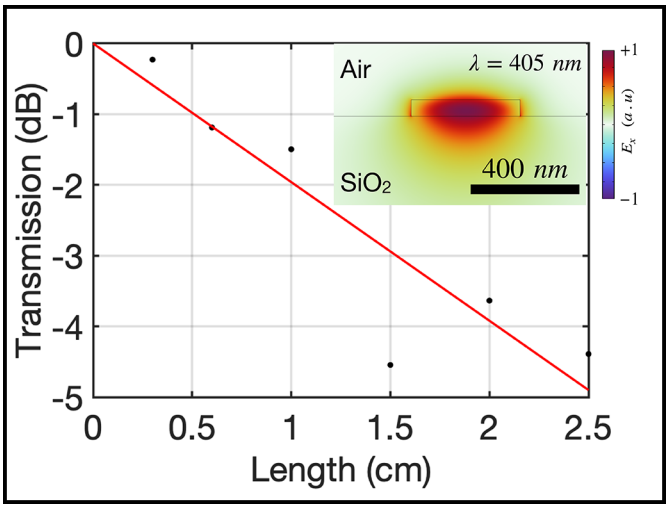

Figure 3: Measured fiber-fiber transmission at λ = 405 nm as a function of propagation length for a 200 by 60 nm waveguide. Points represent measured values, the slope of the fit indicates propagation losses of 1 dB/cm. Inset: Mode profile of measured transmission.

3 mm of thermally grown wet silicon oxide (SiO_2) provided by Rogue Valley Microdevices. Composite films of HfO_2 and Al_2O_3 at DC = 0.33 and P = 3 layers deposited at CNF exhibited material losses of 8 dB/cm at λ = 405 nm (<2 dB/cm at λ = 730 nm) after initial deposition and 2.8 dB/cm at λ = 405 nm (< 1 dB/cm at λ = 730 nm) after a one hour anneal at 800°C.

Test structures to measure propagation losses in SM rectangular waveguides were designed, including fiber surface grating couplers for characterization at λ = 730 nm and at λ = 405 nm. The pattern was defined with electron-beam lithography (JEOL9500) using ZEP520-A resist, and then transferred to the composite material with an inductively coupled plasma (ICP) etching process utilizing a BCl_3/Ar chemistry.

Figure 2 shows an SEM image of the resulting profile for straight waveguide strips in the composite after etching. Preliminary measurements on the resulting structures show losses of 1.9 ± 1 dB/cm for λ = 405 nm in a nominally 400 × 60 nm waveguide with top air cladding (Figure 3). Accounting for a confinement factor of ~33%, we find that propagation losses arising from surface roughness in a patterned waveguide contribute about half of the total propagation losses. SiO_2 cladding is expected to further reduce losses from surface roughness scattering, pushing waveguide transmission to be predominantly limited by the material.

Conclusions and Future Steps:

This work shows that HfO_2 /Al_2O_3 composite layers can be patterned into low-loss and high index integrated photonic structures, enabling high index contrast devices in the visible and UV. Improvement on sidewall roughness and etch profile is in progress, and future work will assess the ultimate material loss limit in this platform. This work may lead to significantly more efficient grating devices, compact footprints, and microresonant structures, among others, for photonics at blue/UV wavelengths as compared to platforms in pure Al_2O_3. High index, deposited waveguide core materials are also likely to be enabling in active electro- and acousto-optic device configurations.

References:

[1] Daniel J. Blumenthal. Photonic integration for UV to IR applications. APL Photonics 5, 020903, 2020.

[2] Galan Moody, et al. Roadmap on integrated quantum photonics. J. Phys. Photonics 4 012501. 2022.

[3] Mehta, K., Bruzewicz, C., McConnell, R., et al. Integrated optical addressing of an ion qubit. Nature Nanotech 11, 1066-1070, 2016.

[4] Gavin N. West, William Loh, Dave Kharas, Cheryl Sorace-Agaskar, Karan K. Mehta, Jeremy Sage, John Chiaverini,and Rajeev J. Ram. Low-loss integrated photonics for the blue and ultraviolet regime. APL Photonics 4, 026101, 2019.

[5] L. Kang, B. H. Lee,W.-J. Qi, Y. Jeon, R. Nieh, S. Gopalan, K. Onishi, and J. C. Lee. Electrical characteristics of highly reliable ultrathin hafnium oxide gate dielectric. IEEE Electron Device Letters, vol. 21, no. 4, pp. 181-183, 2000.

[6] P. Torchio, A. Gatto, M. Alvisi, G. Albrand, N. Kaiser, and C. Amra. High-reflectivity HfO_2/SiO_2 ultraviolet mirrors. Applied Optics, vol. 41, no. 16, pp. 3256-3261, 2002.

[7] Zhang, C., Divitt, S., Fan, Q. et al. Low-loss metasurface optics down to the deep ultraviolet region. Light Sci Appl 9, 55, 2020.

[8] Leonardo Massai. High Polarization Purity and Short-wavelength Optics for Trapped-ion Quantum Systems. Master's thesis, ETH, 2021.

Metamaterial Spectrometer: A Low SWaP, Robust, High Performance Hyperspectral Sensor for Land and Atmospheric Remote Sensing

CNF Project Number: 3003-22
Principal Investigator & User: Lori Lepak

Affiliation(s): Phoebus Optoelectronics LLC
Primary Source(s) of Research Funding: National Aeronautics and Space Administration (NASA)
Contact: llepak@phoebusopto.com
Website(s): www.phoebusopto.com
Primary CNF Tools Used: ASML DUV stepper, Oxford ALD / PECVD / 81 etcher, Logitech CMP, Supra SEM

Abstract:

Since 2003, Phoebus Optoelectronics has enabled custom R&D solutions in the fields of Plasmonics, Metamaterials, Antennas, and Sensors. We work closely with our customers throughout device development, from simulation and design, to prototype realization, testing, and small volume manufacturing. Our R&D portfolio spans the spectral ranges of visible light, infrared, THz, and microwave radiation, for applications in high resolution imaging systems, wavelength and polarization filtering, tunable optical components, beam forming and steering, solar cells, renewable energy devices, and chemical and biological toxin sensors. We routinely partner with large, industry-leading businesses to develop products in all of these areas, jointly performing advanced testing and working together to scale up to medium- and large-volume manufacturing. Our agile team makes extensive use of the resources at the CNF for our nano/micro fabrication and testing, to provide cost efficiency and rapid turnaround.

In the present report, we discuss the ongoing development of a metamaterial-based hyperspectral imaging filter.

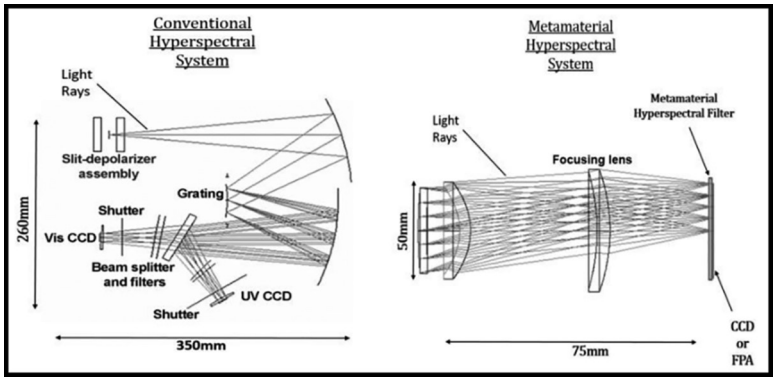

Figure 1: Phoebus's Metamaterial Spectrometer (MS) technology (right) eliminates much of the size and weight of conventional hyperspectral spectrometer technologies (left). Note the significant difference in scale of the two images.

Summary of Research:

Phoebus uses the resources of the CNF to fabricate plasmonic chips patterned with a metamaterial surface to enable Extraordinary Optical Transmission (EOT), a phenomenon unique to metastructures in which light is transmitted through apertures much smaller than the incident wavelength, at anomalously large intensities relative to the predictions of conventional aperture theory. EOT was first observed by T.W. Ebbesen in 1998 [1]. Since its founding in 2003, Phoebus has successfully harnessed EOT by incorporating metasurfaces into devices used to perform light filtering [2-3], photon sorting [4-5], polarimetric detection [6], high speed optical detection [7], and SPR plasmonic sensor chips [8].

In our current project, we are developing a hyperspectral imaging system, shown schematically in Figure 1. Our technology (Figure 1b) uses a metasurface to precisely target very narrow spectral bands of interest, enabling a significant reduction in the size and number of optical components relative to current state-of-the-art imaging systems (Figure 1a), which in turn will enable the integration of our high-performance sensor onto weight-sensitive platforms (ie. satellites) far more readily than existing systems. Our initial goal is to detect and image trace gases in the Earth's atmosphere in the midwave infrared (MWIR), defined as 3-5 μm wavelength, while minimizing dependence on the Angle of Incidence (AoI) of light upon the sensor, up to an angle of 12° off-normal.

Using the ASML DUV stepper, entire wafers can rapidly be lithographically patterned with highly uniform, large-area arrays of metastructures, as shown in Figure 2. In general, the optimal feature size and period of these metastructures depends primarily upon the desired

wavelength of operation and the refractive indices of the constituent materials. In the MWIR, typical feature sizes are on the order of ~ 1 μm. Equally critical for minimizing optical losses in photonics applications, the relatively narrow spaces between features can be etched to form high-aspect-ratio structures with nearly vertical sidewalls, as shown in Figure 3.

Conclusions and Future Steps:

With strong, ongoing support from the National Aeronautics and Space Administration (NASA), we have successfully tested our second generation MWIR devices. As shown in Figure 4, they demonstrated the desired AoI insensitivity up to 12°. As we finish optimizing a few key process improvements in our third generation devices, we are beginning to develop a fourth generation design, in which we will fully optimize and pixelate our MWIR device. In addition, we are adapting our metasurface technology to other spectral ranges, from the visible to the microwave, by substituting appropriate materials, and scaling feature sizes as appropriate to the imaging wavelength. The extensive resources of the CNF are enabling us to rapidly develop our Metamaterial Spectrometer technology for a broad range of imaging and sensing applications.

References:

[1] Ebbesen, T.W., et al., "Extraordinary optical transmission through sub-wavelength hole arrays." Nature, (1998). 391(6668): p. 667-669.

[2] Crouse, D. "Numerical modeling and electromagnetic resonant modes in complex grating structures and optoelectronic device applications." Electron Devices, IEEE Transactions on 52.11 (2005): 2365-2373.

[3] Crouse, D., and Keshavareddy, P. "Polarization independent enhanced optical transmission in one-dimensional gratings and device applications." Optics Express 15.4 (2007): 1415-1427.

[4] Lansey, E., Crouse, D., et al. "Light localization, photon sorting, and enhanced absorption in subwavelength cavity arrays." Optics Express 20.22 (2012): 24226-24236.

[5] Jung, Y.U; Bendoym, I.; Golovin, A.B.; and Crouse, D.T. "Dual-band photon sorting plasmonic MIM metamaterial sensor." Proc. SPIE 9070, Infrared Technology and Applications XL, 90702X (June 24, 2014); doi:10.1117/12.2050620.

[6] Crouse, D., and Keshavareddy, P. "A method for designing electromagnetic resonance enhanced silicon-on-insulator metal-semiconductor-metal photodetectors." Journal of Optics A: Pure and Applied Optics 8.2 (2006): 175.

[7] Mandel, I.; Gollub, J.; Bendoym, I; Crouse, D. Theory and Design of A Novel Integrated Polarimetric Sensor Utilizing a Light Sorting Metamaterial Grating. Sensors Journal, IEEE, (2012): Vol. PP, 99

[8] Lepak, L., et al. "Handheld chem/biosensor using extreme conformational changes in designed binding proteins to enhance surface plasmon resonance (SPR)" Proc. SPIE 9862, Advanced Environmental, Chemical, and Biological Sensing Technologies XIII, 9862-7 (April 17, 2016); doi:10.1117/12.2222305.

[9] Bendoym, I., Lepak, L., Leitch, J., Applegate, J., Crouse, D. "Low SWaP-C hyperspectral metamaterial spectrometer (MMS) for narrow-band, wide angle-of-incidence MWIR atmospheric sensing," Proc. SPIE 12091, Image Sensing Technologies: Materials, Devices, Systems, and Applications IX, 120910J (30 May 2022); https://doi.org/10.1117/12.2632794

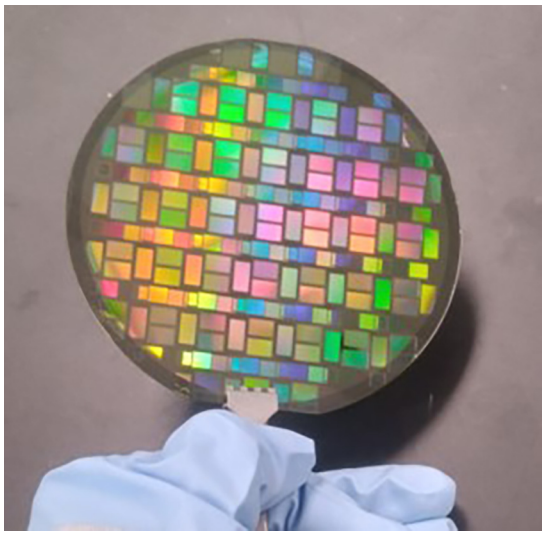

Figure 2: Wafer lithographically patterned with optical metastructures, using the ASML DUV stepper.

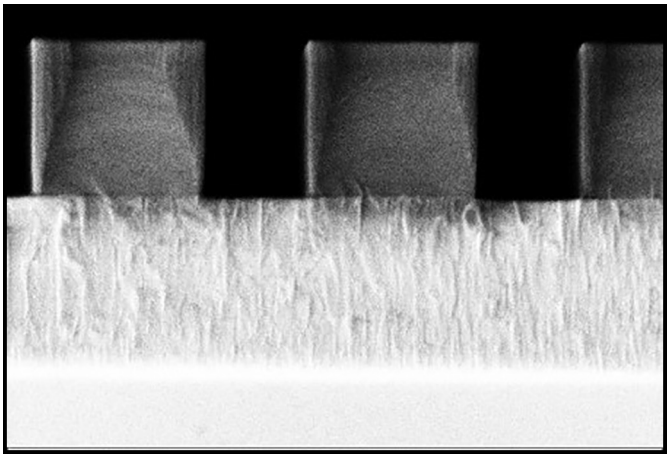

Figure 3: SEM image (cross section) of etched pillars with near-vertical sidewalls. Imaged at ~90kX in the Supra SEM, the grain structure of the etch stop layer is clearly visible.

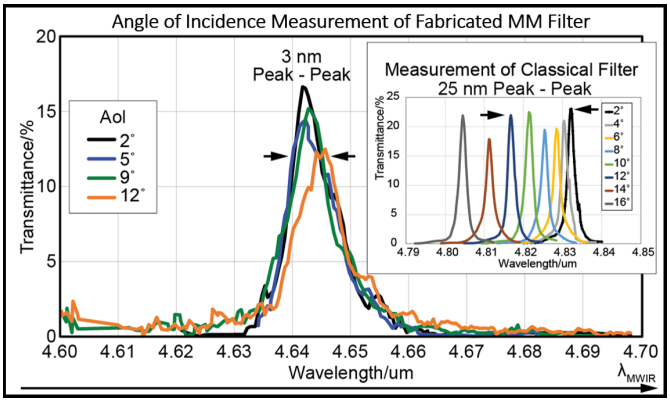

Figure 4: Measured optical performance of fabricated metamaterial filter showing the angle of incidence independence up to a cone of 12° (f/2.4). (Inset) Same measurement performed on a classical Fabry-Pérot filter. Reproduced from reference 9.

Distributed Bragg Reflectors Fabricated by Plasma-Enhanced Chemical Vapor Deposition

CNF Project Number: 3077-23
Principal Investigator(s): A. Nickolas Vamivakas[1], Todd D. Krauss[1,2]
User(s): Robert Collison[1]

Affiliation(s): 1. The Institute of Optics, University of Rochester, Rochester, NY, United States; 2. Department of Chemistry, University of Rochester, Rochester, NY, United States

Primary Source(s) of Research Funding: National Science Foundation, Centers for Chemical Innovation, Award Number CCI-2124398: Quantum Electrodynamics for Selective Transformations (CCI QuEST)

Contact: nick.vamivakas@rochester.edu, todd.krauss@rochester.edu, rcolliso@ur.rochester.edu

Website(s): https://www.rochester.edu/quest/

Primary CNF Tools Used: Oxford PECVD, PT Takachi HDP-CVD, Woollam Ellipsometer, FilMetrics F40-UV, SC-4500

Abstract:

Distributed Bragg Reflectors (DBRs) are mirrors composed of alternating layers of two different transparent materials with different refractive indices (n). When two parallel DBRs are separated by a transparent spacer layer, a Fabry-Pérot microcavity is formed. In such a cavity, the Q-factor of the cavity's resonant mode increases with the reflectivity of the DBRs. Thus, in order to create microcavities with high Q-factors, we tested several designs and compared the reflectance spectra of the resulting DBRs to determine which design produces the highest reflectance at the desired wavelengths.

Summary of Research:

Unlike metal mirrors that reflect light across a broad range of wavelengths, the high-reflectance of a DBR is limited to range of wavelengths known as a stopband. These are the wavelengths of light that are strongly reflected (e. g. reflectance R ≥ 0.99) by a DBR due to the constructive interference of the light scattered from the interfaces between the high- and low-index materials [1]. To make a DBR that reflects strongly at a certain wavelength, λ_{center}, at normal incidence, the layers are fabricated with thickness $d = \lambda_{center}/4n$ (Figure 1). With a sufficient number of layers (roughly 15 or more), a DBR thus fabricated will exhibit high reflectance at normal incidence over a range of wavelengths around λ_{center}. For example, a 31-layer DBR made with λ_{center} = 500 nm reflects light strongly (with R ≥ 0.95) from about 450 to 550 nm. Outside of this stopband region, the reflectance of the DBR is low and varies sinusoidally with wavelength, as shown in Figure 2(a).

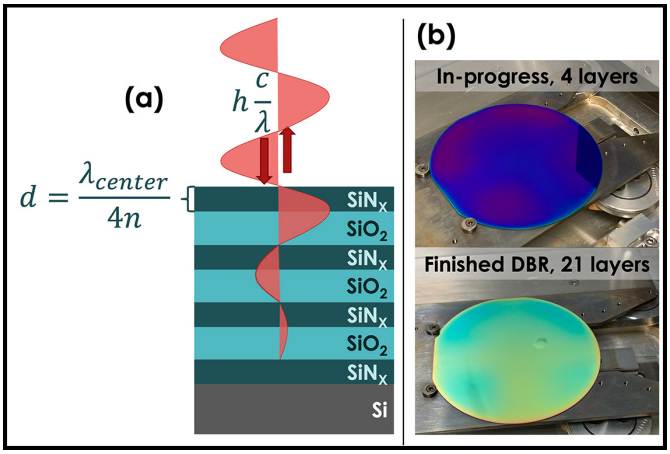

Figure 1: (a) DBR reflection at normal incidence. The impinging light wave is reflected due to the constructive interference of the individual reflections from each SiN_x/SiO_2 interface. (b) The reflection spectrum and color of the SiN_x/SiO_2 film stack on an Si wafer changes radically as layers are added during the deposition of a 21-layer DBR on Si with λ_{center} = 580 nm.

We tested several DBR designs and compared the resulting spectra. DBRs made of alternating layers of silicon nitride (SiN_x) and silicon oxide (SiO_2) were deposited using the Oxford plasma-enhanced chemical vapor deposition (PECVD) instrument. These DBRs were deposited onto 4-inch wafers of SiO_2, Si, or Si that had been coated with 200 nm of Ag in the SC4500 electron-beam evaporator.

We compared of Si- to Ag-backed DBRs (Figure 2) to determine if Ag-backed DBRs would exhibit greater reflectivity than the Si-backed DBRs, as was reported in the literature for 20-layer DBRs [2]. However, we found that, for 31-layer DBRs, the Ag-backed DBRs were not significantly more reflective than the Si-backed DBRs (Figure 2(a)). The simulated reflection spectra calculated using the transfer matrix method (TMM) likewise indicates that the Ag-backed DBR is not expected to reflect more strongly than the Si-backed DBRs for 31-layer DBRs (Figure 2(b)).

In other words, since the reflectivity of a 31-layer DBR is essentially "saturated" within the stopband region due to the constructive interference of the reflections from

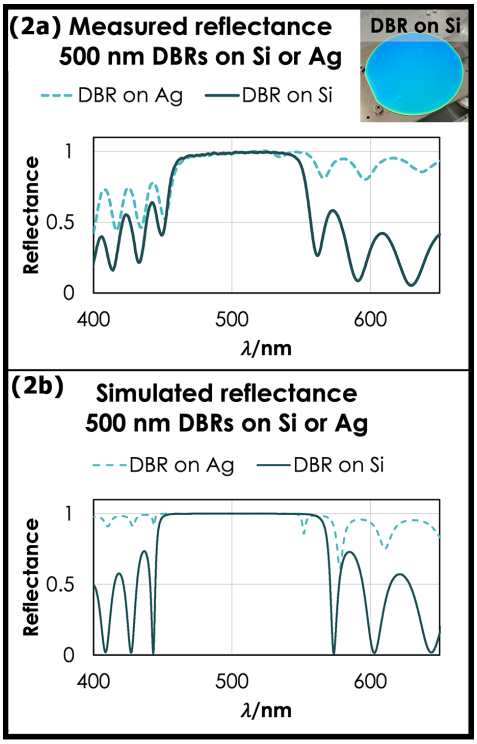

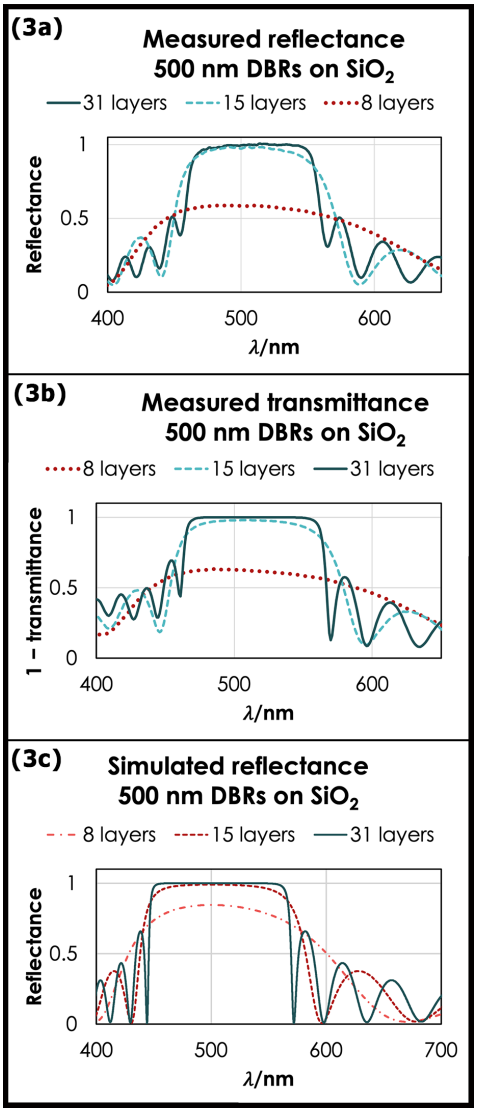

each SiO_2/SiN_x interface, no significant increase in the reflection from the underlying Ag film could be observed. Additionally, the simulated spectrum shows a distinct dip in the reflectance in the DBR stopband for the Ag-backed DBRs due absorption of light into the Tamm plasmon mode [3]. This dip is also present in the experimental reflection spectrum of the Ag-backed DBR, but the absorption peak is much less distinct in the measured spectrum than in the simulated data. This might also be due to the "saturation" of the DBR reflectance for these materials at 31 layers, such most of the impinging light in the stopband region does not reach the Ag film underneath the DBR.

We also compared the spectra of DBRs having various numbers of SiN_x and SiO_2 layers deposited on SiO_2 wafers (Figure 3). Since these samples were deposited on transparent substrates, both their reflection and their transmission spectra were measured and compared (Figure 3). The spectra show that 8 layers is too few to make a highly reflective ($R > 0.95$) DBR; that 15 layers makes a DBR with low, but non-zero, transmittance in the stopband region; and that, for 31 layers, the transmittance in the stopband region is at or below the background noise level of the spectrometer (Woollam RC2 Ellipsometer, operated in the transmission configuration). Note that these conclusions are essentially qualitative. To precisely quantify the DBRs' transmittance in the stopband region would require measurement of the reflected and transmitted light using lasers or supercontinuum white light sources.

Acknowledgements:

We thank the NSF for supporting this work as part of The Center for Quantum Electrodynamics for Selective Transformations (CCI-2124398). We would also like to thank the CNF staff, especially Jeremy Clark for his assistance with the Oxford PECVD, Alan Bleier for his assistance with the Woollam RC2 Ellipsometer, and Aaron Windsor for assistance on the electron-beam evaporator. Finally, we thank Mitesh Amin at The University of Rochester for authoring the MATLAB script used to simulate the DBR reflection spectra.

References:

[1] Maxwell Rules - Distributed Bragg Reflectors. http://maxwellrules.com/meep/distributed_bragg_reflector.html (accessed 2022-10-03).

[2] McGhee, K. E., et al. Polariton Condensation in an Organic Microcavity Utilising a Hybrid Metal-DBR Mirror. Sci. Rep. 2021, 11 (1), 20879. https://doi.org/10.1038/s41598-021-00203-y.

[3] Li, L.; Hao, H. Evolution of High-Order Tamm Plasmon Modes with a Metal-PhC Cavity. Sci. Rep. 2022, 12 (1), 14921. https://doi.org/10.1038/s41598-022-19435-7.

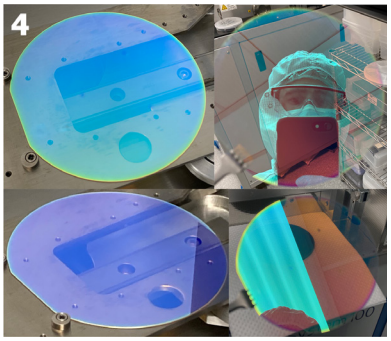

Figure 2, top left: *λ_{center} = 500 nm DBRs on Si or Ag. (a) DBR reflection spectra measured on the Filmetrics F40-UV. Inset: a photo of the 500 nm DBR on Si. (b) Simulated DBR reflection spectra calculated by TMM.* **Figure 3, bottom left:** *(a) Reflection and (b) transmission spectra of 500 nm DBRs with various layer numbers on SiO_2 wafers, measured using the Filmetrics F40-UV and Woollam RC2 Ellipsometer, respectively. (c) Simulated DBR reflection spectra calculated by TMM.* **Figure 4, above:** *31-layer 500 nm DBR on SiO_2. The transparent substrate allows the DBR's opalescence to be observed, as shown by the photos on the right, in which reflected light is cyan and transmitted light is orange or rose-colored.*